Multi-satellite observed responses of precipitation and its extremes to interannual climate variability

Article

Accepted Version

Formatted: Numbering: Continuous

Multi-satellite observed responses of precipitation and its extremes to interannual climate variability

Chunlei Liu and Richard P. Allan

Department of Meteorology, University of Reading, Reading, UK

ABSTRACT

The consistency of precipitation variability estimated from the multiple satellite-based observing systems is assessed. There is generally good agreement between TRMM TMI, SSM/I, GPCP and AMSRE datasets for the inter-annual variability of precipitation since 1997 but the HOAPS dataset appears to overestimate the magnitude of variability. Over the tropical ocean the TRMM 3B42 dataset produces unrealistic variability~~s~~. Based upon deseasonalised GPCP data for the period 1998-2008, the sensitivity of global mean precipitation (P) to surface temperature (T) changes (dP/dT) is about 6%/K, although a smaller sensitivity of 3.6%/K is found using monthly GPCP data over the longer period 1989-2008. Over the tropical oceans dP/dT ranges from 10-30%/K depending upon time-period and dataset while over tropical land dP/dT is –8 to –11%/K for the 1998-2008 period.

Analyzing the response of the tropical ocean precipitation intensity distribution to changes in T we find the wetter area P shows a strong positive response to T of around 20%/K. The response over the drier tropical regimes is less coherent and varies with datasets, but responses over the tropical land show significant negative relationships over an interannual time-scale. The spatial and temporal resolutions of the datasets strongly influence the precipitation responses over the tropical oceans and help explain some of the discrepancy between different datasets. Consistency between datasets is found to increase on averaging from daily to 5-day time-scales and considering a 1^{o} (or coarser) spatial resolution. Defining the wet and dry tropical ocean regime by the 60^{th} percentile of P intensity, the 5-day average, 1^{o} TMI data exhibits a coherent drying of the dry regime at the rate of -20%/K and the wet regime becomes wetter at a similar rate with warming.

1. Introduction

Climate change is anticipated to exert profound effects on the hydrological cycle and therefore society [*Meehl et al.*, 2007]. Anticipated changes, based upon physical theory and global modeling have long indicated increases in global mean precipitation, intensification of extreme precipitation and a decline in mean precipitation over the dry, sub-tropical regions of net moisture export [*Mitchell et al.*, 1987; *Trenberth*, 2011]. While enhanced radiative cooling of a warming atmosphere is thought to control global mean changes [*Mitchell et al.*, 1987; *Lambert and Webb*, 2008; *Stephens and Ellis*, 2008; *Allan*, 2009], regional changes in mean and extreme precipitation are strongly linked to the rises in atmospheric moisture with warming due to the Clausius Clapeyron equation [*Emori and Brown*, 2005; *Bengtsson et al*., 2007] which explains enhanced transport of moisture into regions of net moisture convergence [*Held and Soden*, 2006], and also changes in dry static energy transport [*Muller and O'Gorman*, 2011].

Appreciating the robust aspects of changes in global to regional precipitation changes are vital for informing adaptation and mitigation policy choices and therefore there is a powerful motivation for confirming physically based models by careful use of high quality, homogenous observations. Observed signals of increased global mean and extreme precipitation and an enhanced contrast between the wet and dry regions of the tropics have been detected [*Zhang et al.*, 2007; *Chou et al*., 2007; *Adler et al.*, 2008; *Allan et al.*, 2010; *Min et al.*, 2011] yet obtaining consistent and robust results from a variety of observing systems remains a considerable challenge [*John et al.*, 2009; *Haerter et al*., 2010; *Wang et al.*, 2008].

The aim of the present study is to evaluate the observed global response of precipitation and its extremes utilizing a variety of satellite-based global datasets over a range of spatial and temporal scales. The reason for doing so is to seek clear observational signals of precipitation response to natural cycles of warming and cooling in the present day climate system that may be of relevance for evaluating the physical responses simulated in a variety of climate model simulations and identifying reasons for inconsistencies among datasets. We consider global data from 1987 to 2010 but concentrate upon the period since 1997 over the tropical region (30^{o}N-30^{o}S), since it not only has the main ascending branch of the Hadley and Walker circulations which affect the climate globally, but it is also covered by a variety of satellite observations. The two primary questions we aim to address in the following sections are: (i) are there robust responses of global and tropical precipitation and its percentile distribution to interannual changes in surface temperature and (ii) how do the spatial and temporal scales sampled influence these relationships.

2. Datasets and methods

Ideally, observed precipitation data over the whole globe will be helpful in studying the spatial distribution of precipitation and its response to changing climate, but few datasets covering both the global land and ocean are available. Most satellites sensors may only reliably retrieve precipitation over the ice-free oceans.

The SSM/I (Special Sensor Microwave Imager) is a seven-channel, four-frequency, orthogonally polarized, passive microwave radiometric sensor system [*Wentz and Spencer*, 1998; *Vila et al.*, 2010] covering the global ice-free ocean and it has been operated on different DMSP (Defense Meteorological Satellite Program satellites) platforms (F08, F10, F11, F12, F13 and F15) since 1987. It has a spatial sampling resolution from 12.5 to 25km. The precipitation rate is one of the retrieved parameters. The next generation SSM/I instrument, the Special Sensor Microwave Imager/Sounder (SSMIS) [*Wentz and Spencer*, 1998] on aboard DMSP satellites F16 and F17 has been operating since 2003 and 2007 respectively. The precipitation rates are retrieved using new algorithms and the SSMIS data have been carefully intercalibrated on the brightness temperature level with the previous SSM/I (see http://www.ssmi.com/ssmi/ssmi_description.html for details). It is noted that both F16 and F17 datasets have some calibration problems and are under reprocessing (Smith, personal communication, 2011); we include them here for comparison purposes only.

HOAPS (Hamburg Ocean Atmosphere Parameters and Fluxes from Satellite Data) dataset [*Andersson et al.*, 2010] contains a completely reprocessed time-series of global ocean freshwater flux related parameters using variables derived from SSM/I data over the ice free global ocean ranging from 1987 to 2005.

The AMSRE (Advanced Microwave Scanning Radiometer - Earth Observing System) [*Lobl*, 2001] instrument measures geophysical fields related to the earth's water cycle including precipitation rate over the global ice-free ocean. The AMSRE dataset is retrieved from a twelve-channel, six-frequency, passive microwave radiometer which has a spatial sampling interval from 5 km to 10 km. The spatial resolution of AMSRE data is double that of SSM/I data.

The TRMM 3B42 (Tropical Rainfall Measuring Mission) [*Huffman et al.*, 2007] dataset is a TRMM adjusted merged-infrared (IR) precipitation dataset using multi-satellite datasets including TMI (TRMM Microwave Imager), SSM/I, AMSR and AMSU (Advanced Microwave Sounding Unit). It covers both the tropical ocean and the tropical land (50^{o}N - 50^{o}S). The TMI is a nine-channel passive microwave radiometer based on SSM/I and has spatial sampling resolution about 14km. The TMI dataset is well-calibrated and contains precipitation rate over the tropical ocean only (40^{o}N - 40^{o}S) [http://www.ssmi.com/tmi/tmi_description.html]. The global ocean and land are only covered by the

merged GPCP (Global Precipitation Climatology Project) dataset containing data from land-based rain-gauges, sounding observations, microwave radiometers (such as SSM/I) and infrared radiances from the Global Precipitation Climatology Centre [*Adler et al.*, 2003].

The data period available for this study and their properties are listed in Table 1. Not all of these datasets listed in Table 1 are independent. For example, the SSM/I dataset is used by the GPCP, HOAPS and TRMM 3B42 datasets and the TMI dataset is also used by the TRMM 3B42 dataset. On the other hand, the TRMM satellite is not sun-synchronous and is on a low inclination orbit, the SSM/I and SSMIS satellite are on sun-synchronous and near-polar orbits. The AMSRE satellite is also on a sun-synchronous orbit. The sun-synchronous orbiter only dataset can simply miss some parts of the diurnal cycle, which can be significant even over the ocean. All datasets used in this study provide daily data including zero precipitation rates. However, the satellite measurements do not provide daily averaged quantities and rather sample instantaneous rainfall rates over 2 overpasses per day and therefore may be considered as instant snap-shots of the precipitation fields averaged over the satellite footprints, averaged up to the regular grids.

Table 1. Precipitation datasets and their properties.

Dataset	Period	Description
GPCP 1DD v1.1	1996 – 2009	Combined observed precipitation from satellite and rain gauges. Daily data, global ocean and land, 1° resolution. (SSM/I) (http://www.gewex.org/gpcpdata.htm)
AMSRE v5	2002 – present	Twice a day, global ice-free ocean, 0.25° resolution. (http://nsidc.org/data/amsre/)
SSM/I v6 F08 F11 F13	 1987 – 1991 1992 – 2000 1995 – 2009	Twice a day, global ice-free ocean, 0.25° resolution. (http://www.remss.com/ssmi/ssmi_description.html)
SSMIS v7 F16 F17	 2003 – present 2006 – present	Twice a day, global ice-free ocean, 0.25° resolution. (http://www.remss.com/ssmi/ssmi_description.html)
TMI v4	1997 – present	1 to 2 times per day, ~~Twice a day,~~ tropical ocean only (40°N -40°S), 0.25° resolution. (http://www.remss.com/tmi/tmi_description.html)
HOAPS v3	1987 – 2005	Twice a day, global ice-free ocean, 1° resolution. (SSM/I) (http://www.hoaps.zmaw.de/)
TRMM 3B42 v6	1998 – present	Tropical ocean and land (50°N -50°S), 0.25° resolution. (TMI, SSM/I, AMSR, AMSU, IR), daily and 3 hourly. (http://trmm.gsfc.nasa.gov/3b42.html)
GPCP v2.2 monthly	1979 - 2008	As GPCP v1.1, but it is monthly, 2.5° resolution.
ERA INTERIM	1989 - present	6 hourly, global, 0.25° resolution.

All products considered have a spatial resolution of 0.25^o except for GPCP and HOAPS datasets which have a resolution of 1^o. The low resolution (2.5^o) monthly GPCP dataset is also listed for comparison purpose because it is available over a longer time period (1979-2008). We only consider the period containing microwave measurements since 1987. The SSM/I dataset used in this study consists of joint data from three satellite platforms, F08, F11 and F13, and they are treated as one time series without any adjustment. Since the time when F13 satellite passes the equator drifts least, so all F13 data from 1995 to 2009 are used, together with all F08 data from 1987 to 1991 [*Gastineaux and Soden*, 2011]. The gap between F08 and F13 (1992-1994) is filled by F11 data. The surface temperature considered is air temperature at 2m from the European Centre for Medium-range Weather Forecasts (ECMWF) INTERIM reanalysis [*Dee et al.*, 2011] which is accumulated from six hourly data having resolution of 0.25^o interpolated from the original N128 reduced Gaussian grid ($\sim 0.7^o$).

In order to study the precipitation (P) variation and its relationship with the surface temperature (T), P is also divided into percentile bins in ascending order calculated from all valid data points in a month, and the anomaly time series of P averaged over the percentile bin is calculated for each percentile bin. The anomaly time series of the global or tropical area average T is also calculated and the linear least squares fit gradient, dP/dT, is computed using a similar approach to *Allan et al.* [2010]. The precipitation percentile bin intervals used for this study are 10% from 0 to 60% (6 bins), then 5% from 60 to 80% (4 bins) and then every 1% from 80 to 100% (20 bins). This choice was made to account for the substantial number of dry grid points that dominate the lowest percentiles and also to contain a sufficient number of bins to capture the long tail in the distribution at high rain rates.

To study the effect of temporal resolution on the observed P-T relationships, the daily data is also integrated to 3 days, 5 days, 10 days and monthly data respectively. Then the integrated precipitations over a month are used for the percentile bin calculation. dP/dT is then obtained from the gradient of the P and T anomaly regression. For the spatial integration, the 0.25^o data are integrated to 1^o, 2^o and 4^o resolutions respectively. In both temporal and spatial integrations, the total mean precipitation rates are kept same.

3. Seasonal and interannual variability in global and tropical Precipitation

To check the consistence of the precipitation rate in the observed datasets from different satellite platforms, the mean precipitation over the whole globe, the tropical ocean and the tropical land, are calculated from each dataset based on the reference period of 2003-2008, except for the HOAPS dataset (based on 2000-2005), SSMIS F16 dataset (based on 2004-2009) and the SSMIS F17 dataset (based on 2007-2010), due to data period limitations. Zero precipitations are all included in our calculations.

Only the GPCP dataset covers both the global ocean and land. In order to test the sensitivity of global precipitation variability to dataset, we also generated some hybrid global datasets using global ice-free ocean data from the AMSRE, SSM/I, HOAPS and SSMIS F16 datasets. The high resolution (0.25^{o}) ocean data are integrated to 1^{o} resolution and all missing values (including those over the land and the ice-covered oceans) are simply filled with daily GPCP data. The mean precipitation and the corresponding anomalies are calculated at 1^{o} resolution for hybrid datasets and at original resolutions for other datasets listed in Table 1. It is not our aim here to construct new datasets but merely to assess the sensitivity of global precipitation and its variability to the choice of satellite dataset applied over the oceans.

Mean surface temperature from ERA INTERIM and mean precipitation from all datasets listed in Table 1 are plotted in Figure 1. Both global and land temperatures (Figure 1a) show strong seasonal variations.

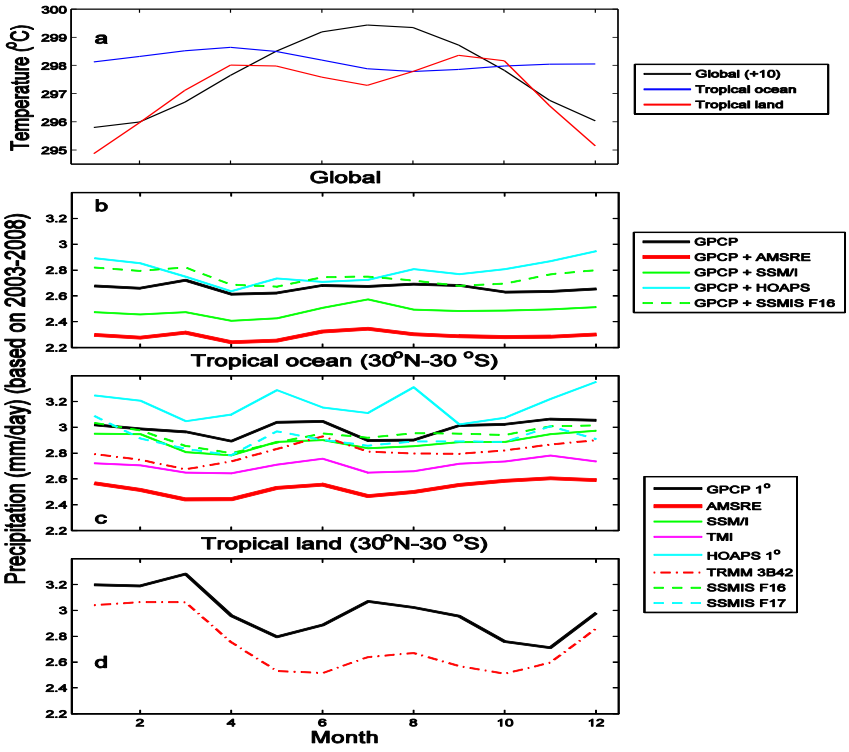

Figure 1. Mean seasonal cycle of. (a) temperatures over the globe, the tropical ocean and the tropical land based on the reference period of 2003-2008 (10^{o}C is added to the global temperature to improve the clarity of the plot) and precipitation for different datasets based on the reference period of 2003-2008 except for HOASPS (based on 2000-2005), SSMIS F16 dataset (based on 2004-2009) and the SSMIS F17 dataset (based on 2007-2010) over (b) the globe, (c) the tropical ocean, and (d) the tropical land.

The global mean precipitation calculated from GPCP and the four hybrid global datasets (Figure 1b) show little coherent seasonal variation. There is good agreement between GPCP and the hybrid GPCP+SSMIS F16 dataset and to a lesser extent the GPCP+HOAPS dataset; their mean values are between 2.6 to 2.8 mm/day. Mean precipitation from GPCP+SSM/I and GPCP+AMSRE hybrid datasets are systematically lower than the previous three, and their mean values are around 2.5 and 2.3 mm/day respectively. Because data over the land are the same, so the difference is from the global ice-free ocean. Mean precipitation over

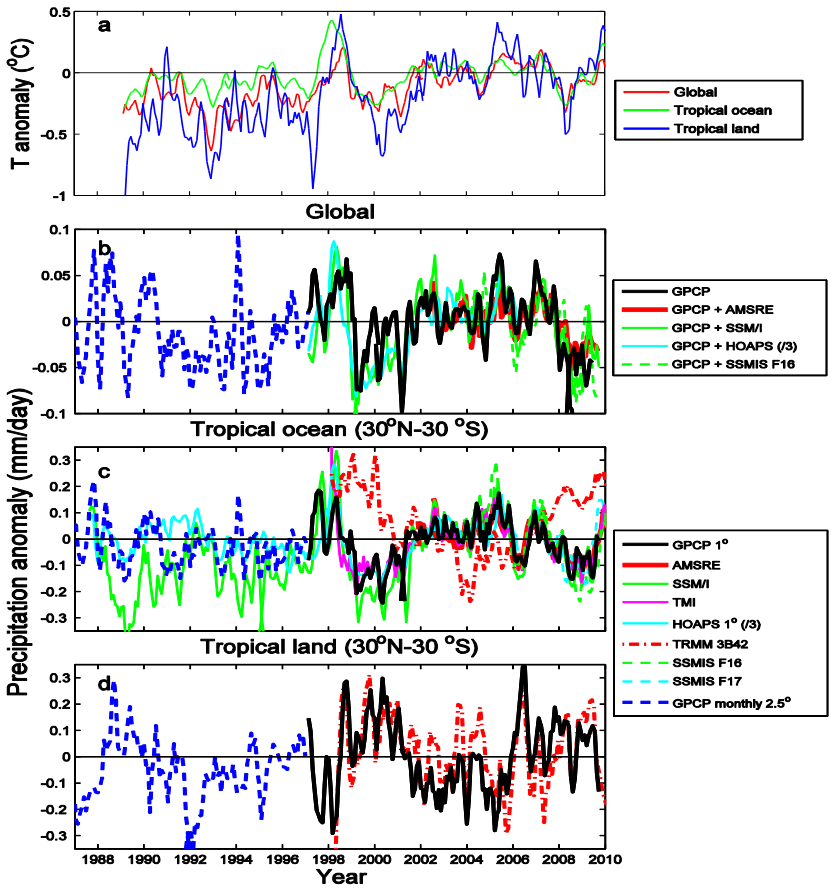

Figure 2. Deseasonalised anomalies of temperature and precipitation relative to the mean values of Figure 1: (a) temperature anomalies at 2m from ERA INTERIM dataset over the globe, the tropical ocean and the tropical land . Precipitation anomalies (b) over the globe, (c) over the tropical ocean, and (d) over the tropical land for all datasets. All curves are plotted with three month running mean. The amplitude of HOAPS precipitation anomalies are scaled down by a factor of 3 to improve the clarity of the plot.

the tropical ocean (30°N-30°S) vary with datasets from 2.5 to 3.4mm/day (Figure 1c). There is good agreement between SSM/I and SSMIS, and they are close to the mean values of all dataset mean precipitation. The seasonal variation for each dataset is small compared with the variation among the datasets. The SSM/I mean precipitation (solid green line) over the tropical ocean is close to that of SSMIS F16, but over the global, it is systematically lower, implying that the difference is from the measurement over the ocean at higher latitude.

There are only two datasets (GPCP and TRMM 3B42) that cover both the tropical ocean and the tropical land. The seasonal variability over the tropical land (30°N-30°S) in Figure 1d is much larger than that over the tropical ocean. Both datasets show similar variability with maximum precipitation around March and minimum precipitation between October and November, though the TRMM 3B42 dataset produces precipitation that is systematically lower by between 0.2 to 0.4 mm/day.

The deseasonalized anomaly time serieses for both temperature and precipitation are plotted in Figure 2. All anomalies are plotted as three month running means. Figure 2a shows the temperature anomalies for the global, tropical ocean and tropical land mean relative to the reference period described in Figure 1. There are strong correlations among them (about 0.7). It clearly shows the decrease after the Pinatubo eruption in June 1991, and the peaks coinciding with El Niño around 1998 and 2005. The temperature increases from 2000 to 2002 and then remains more or less the same for the rest of the period, except during El Niño around 2005 and La Niña around 2008. This covers the most important period of satellite precipitation observations.

The deseasonalized precipitation anomalies (relative to mean precipitations in Figure 1) from different datasets are plotted in Figures 2(b-d). Figure 2b shows the anomalies over the globe. Global mean anomalies from GPCP daily and GPCP monthly datasets are plotted in Figure 2b with the additional four hybrid datasets. Only the GPCP monthly dataset samples prior to 1996. All datasets agree well for the period after 1996, except for the HOAPS dataset which shows a higher amplitude variation and is scaled down by a factor of 3 in the plot. The reasons for this larger variability are currently not clear. The global precipitation anomaly variations have strong correlation with the temperature anomalies in Figure 2a associated with El Niño Southern Oscillation (ENSO).

Over the tropical ocean, there are only three datasets available before 1996, the SSM/I and the HOAPS daily datasets and the GPCP monthly dataset, all of which use the SSM/I data [*Andersson et al.*, 2010; *Adler et al.*, 2008]. There are large differences among datasets before 1992, even between SSM/I and HOAPS datasets. This may because we only used F08, F11 and F13 datasets and HOAPS used all available SSM/I data. All datasets show consistent variability (after the HOAPS anomalies are reduced by a factor of 3) after 1997 except for the TRMM 3B42 dataset which is at odd with the other datasets. This has been reported by *Huffman et al.* [2007] (see their Figure 8) and it is mainly due to the AMSU-B rain estimates because the existing AMSU-B algorithm failed to detect light rain over oceans, particularly in the subtropical highs. This bias will be

corrected in the future dataset version 7 which is expected to be available at the end of 2011 (personal communications, Huffman). Both ENSO events in 1998 and 2005 can be clearly seen from the tropical mean anomalies. Again, the HOAPS anomaly shows higher variability compared to the other datasets and is scaled down by a factor of 3 in the plot.

Over the tropical land shown in Figure 2d, both anomalies from GPCP and TRMM 3B42 datasets follow each other and generally have opposite sign to those over the tropical ocean. The opposite changes in tropical land and ocean precipitation appears to correspond with ENSO, which increases precipitation over the central Pacific and decreases precipitation over South East Asia and Central America, and so may not be simply related to relationships relevant for global warming of climate. The correlation coefficients for GPCP precipitation and ERA INTERIM surface temperature are 0.68 over the tropical ocean and -0.43 over the tropical land. Comparing Figures 2c and 2d implies that the precipitation oscillates between the tropical ocean and the tropical land due to ENSO oscillation. The variations of the anomalies over both the tropical ocean and the tropical land have similar amplitudes.

In order to illustrate the relations between the total P and T anomalies, the scatter plot is shown in Figure 3. The datasets and the period used for this plot are listed in Table 2, together with the gradient $dP_{\%}/dT$ (dP/dT divided by the mean precipitation from Figure 1) and the correlation coefficient (r) which is in bold when significant after applying the two tailed test using Pearson critical values at the level of 5%. For global means (Figure 3a), GPCP and other three hybrid datasets all show positive correlations and the correlations are all significant. The $dP_{\%}/dT$ of these four datasets are between 3.3-8.8%/K. This is consistent with the sensitivity estimated by *Wentz et al.* [2007] who combined SSM/I and GPCP data for the period 1987-2004. The value from our calculations using the monthly mean GPCP dataset over the longer period 1989-2008 is 3.6 %/K, similar to values found by *Adler et al.* [2008] who considered GPCP data for 1988-2006. The value is reduced from 6.0 %/K to 3.6 %/K using the longer GPCP record; this may relate to the data quality before 1998 but also highlights the limitations of considering short records. Our detailed analysis (not shown here) shows the correlation between P and T is strong after 1998 for the monthly GPCP data, but it is very weak before 1998. So the correlation for the longer dataset is reduced. The $dP_{\%}/dT$ values also depend on the corresponding mean precipitation defined in Figure 1 which shows large discrepancies among different datasets.

Over the tropical ocean, the correlations from all five datasets are significant. The values are higher than those for global means. The $dP_{\%}/dT$ values are all above 10%/K and as much as 30%/K for SSMIS F16, similar to but a little higher than the sensitivities calculated by *Allan et al.* [2010] for the 1988-2008 period. *John et al.* [2009] also found a strong dependence of these relationships to dataset and time period considered. Over the tropical land, the correlations are also significant and very close, but they are negative and slightly lower in magnitude than that over the tropical ocean ($dP_{\%}/dT$ is around -8 to -11%/K)

Table 2. Datasets for the scatter plot and the relations between temperature and precipitation anomalies.

	Dataset	Period	$dP_{\%}/dT$ (%/K)	r
Global	GPCP	1998-2008	6.0	**0.56**
	GPCP + AMSRE	2003-2008	4.3	**0.56**
	GPCP + SSM/I F13	1998-2008	8.8	**0.71**
	GPCP + SSMIS F16	2004-2008	3.3	**0.30**
	GPCP monthly	1989-2008	3.6	**0.38**
Tropical ocean	GPCP	1998-2008	14.9	**0.68**
	AMSRE	2003-2010	12.1	**0.62**
	SSM/I F13	1998-2008	25.6	**0.75**
	SSMIS F16	2004-2010	30.9	**0.47**
	TMI	1998-2008	14.9	**0.61**
	GPCP monthly	1989-2008	10.2	**0.48**
Tropical land	GPCP	1998-2008	-8.2	**-0.43**
	TRMM 3B42	1998-2008	-10.6	**-0.46**
	GPCP monthly	1989-2008	-1.1	-0.07

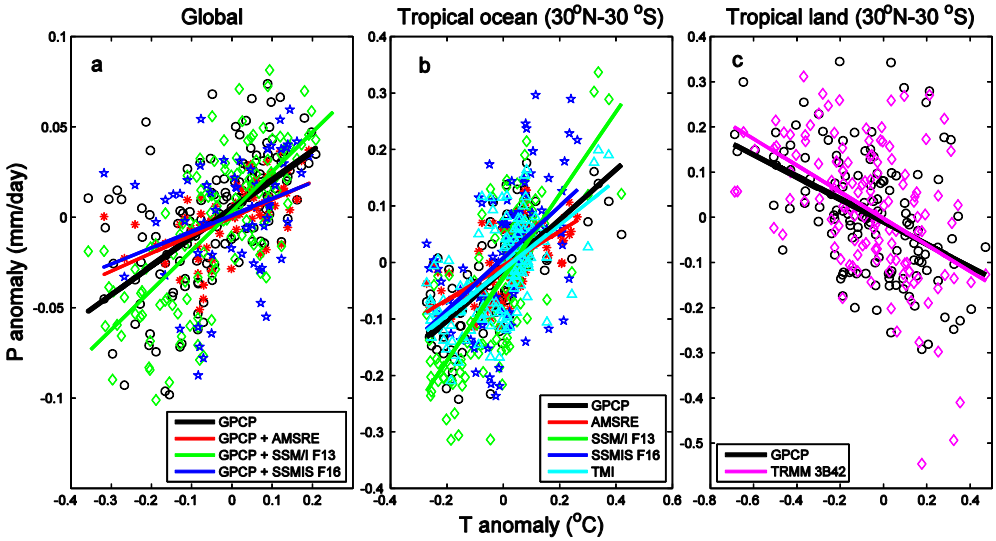

Figure 3. Scatter plot showing correlations between precipitation and temperature anomalies (a) over the global, (b) the tropical ocean and (c) the tropical land.

300 although do not show significant coupling over the 1989-2008 period using monthly GPCP data due to
301 very weak correlation before 1998.
302
303
304 **4. Mean Precipitation over the percentile bins**
305
306 The influence of atmospheric warming upon precipitation extremes is of importance for climate impacts and this
307 motivates the detailed assessment of how the observed precipitation distributions (dry up to the most intense rainfall)
308 respond to temperature [*O'Gorman and Schneider,* 2009; Allan et al., 2010; *Sugiyama et al.*, 2010; Lenderink and
309 van Meijgaard, 2010; *Haerter et al.*, 2010]. In order to quantify changes in the precipitation rate distribution, the
310 mean precipitation for each percentile bin over the tropical ocean is calculated based on the reference period defined
311 for Figure 1. The results are shown in Figure 4. The top row is the mean precipitation from different datasets and
312 integration periods (1 day, 5 day and monthly). All high resolution (0.25^o) datasets are spatially integrated to 1^o
313 resolution in order to compare them consistently. The SSMIS F17 dataset is not used here due to its short
314 observational period. Since zero precipitation is included in all our calculations, for most of the observational
315 datasets, the first few percentile bins contain all zero precipitation. The mean precipitation is not calculated for those
316 bins having zero precipitation at both sides of the bin boundaries. The starting point of each curve in the top row
317 shows where non-zero boundary is reached. The population of zero precipitation points is dataset dependent due to
318 different retrieving algorithms. The difference also becomes smaller as the integration period increases but is
319 particularly prominent for the daily time-scale where the data actually consists of satellite swaths, more comparable
320 to 30-minute sampling [*Wilcox and Donner*, 2007].
321 The difference in precipitation intensity distributions among datasets becomes smaller as the temporal integration
322 period increases, but they are separated into two groups. The purely microwave-based retrievals from AMSRE, TMI
323 and SSM/I produce systematically lower daily precipitation than the blended datasets from GPCP, HOAPS and
324 TRMM 3B42. This discrepancy does not rely on the satellite orbits as discussed in section 2. A possible explanation
325 is that the blended products contain a certain degree of implicit averaging in time and space, thereby increasing the
326 frequency of light rainfall and decreasing the intensity of heavy rainfall. Indeed the differences diminish with greater
327 temporal averaging. There is a near linear increase in logarithmic scale at high percentile bins, but drops quickly at
328 the smaller percentile bins. Of course, this will depend on the definition of bin width. On the other hand, the passive
329 microwave algorithm cannot detect rainfall less than 0.1mm/hr which is why the cut-off values for AMSRE, SSM/I
330 and SSMIS in Figure 4a are much higher than those for blended datasets (GPCP and TRMM 3B42). The small
331 precipitation values in the plot are generated artificially from the average process.

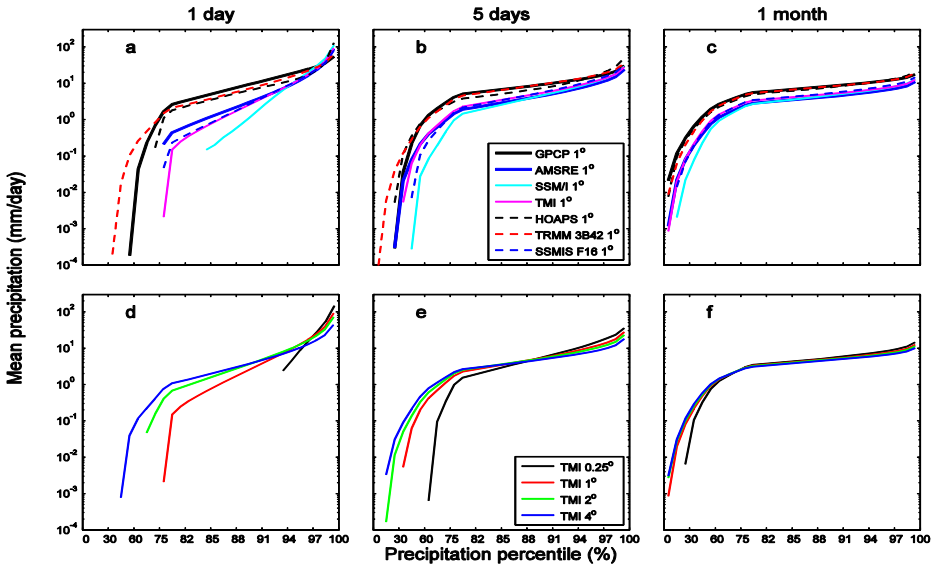

Figure 4. Mean tropical ocean precipitation over the reference period of Figure 1 in different precipitation percentile bins. The upper row is for different datasets at 1° resolution and the lower row is for TMI dataset at different spatial resolutions.

The spatial integration effect on the mean precipitation from the TMI dataset is plotted in the lower row (Figures 4d-f) and it shows that for high resolution (0.25°) the precipitation is zero for most of the light precipitation bins; non-zero precipitation only occurs at very high percentile bins (from the 92nd percentile bin for TMI). Both temporal and spatial integrations reduce the percentage of zero precipitation points. The spatial resolution effect on mean precipitation is also tested for AMSRE and SSM/I datasets (not shown here); they all show similar results to those of TMI. The influence of spatial averaging on the TMI data is to narrow the precipitation distribution, as discussed by *Field and Shutts* [2009]. The mean precipitation values selected from Figure 4, for different precipitation percentile bins of 88-89, 95-96 and 99-100 and integration periods of one day, five days and one month, are listed in Table 3 for the seven datasets in Figure 4. The value for the spatial integration effect of TMI dataset is also listed. For daily data, the mean precipitation varies substantially over different bins and for different datasets. The heaviest precipitation of SSM/I and HOAPS at bin 99-100 are twice that of GPCP. When the time integration period increases, the difference is reduced due to the averaging process. For TMI, the spatial integration greatly reduces the heavy precipitation rate as shown in Table 3: for daily data over the percentile bin of 99-100, the precipitation is reduced from 142 mm/day to 44 mm/day. Figure 4 and Table 3 show that both the temporal

and spatial integrations of the dataset have a profound effect on the precipitation rate distributions as anticipated [*Field and Shutts*, 2009]. Therefore care must be taken in comparing satellite-based estimates of the changes in precipitation percentile distributions with general circulation models. Using an integration period of 5-days produces a more consistent precipitation distribution between datasets with only a small sensitivity to spatial averaging for resolutions of 1 degree and coarser.

Table 3. Mean precipitation (mm/day) in percentile bins for 1 day, 5days and 1 month integration.

	1 day			5 days			1 month		
Percentile bins	88-89	95-96	99-100	88-89	95-96	99-100	88-89	95-96	99-100
GPCP (1^o)	8.0	20.5	52.5	8.8	15.0	31.0	7.6	10.6	16.4
AMSRE (1^o)	2.5	12.2	88.6	6.7	14.8	42.1	7.0	10.6	19.9
SSM/I (1^o)	0.7	14.2	110.8	3.9	9.5	27.7	4.2	6.6	12.3
TMI (1^o)	2.0	13.0	93.1	4.7	10.2	27.3	4.8	7.1	12.4
HOAPS (1^o)	5.6	14.1	127.5	7.1	15.6	56.6	8.1	12.8	24.4
TRMM 3B42 (1^o)	6.1	18.1	61.9	8.1	14.6	33.2	7.4	10.6	17.5
SSMIS f16 (1^o)	2.0	12.5	75.5	4.9	11.5	31.6	5.1	7.8	14.3
TMI (0.25^o)		8.8	142.2	4.5	12.5	34.5	5.2	8.0	14.6
TMI (1^o)	2.0	13.0	93.1	4.7	10.2	27.3	4.8	7.1	12.4
TMI (2^o)	2.9	12.0	67.6	4.7	9.2	23.0	4.5	6.6	11.0
TMI (4^o)	3.2	10.4	44.2	4.5	8.0	18.2	4.2	5.9	9.4

5. Response of precipitation intensity distribution to surface temperature

The response of the intensity distribution of precipitation to climate variability is analyzed in this section. We use the linear least squares sensitivity (dP/dT) of P and T anomalies across percentile bins of P to quantify the response. The relative dP/dT is named $dP_{\%}/dT$ defined as:

$$dP_{\%}(bin)/dT=(1/P(bin))(dP(bin)/dT) \quad (1)$$

where the mean precipitation intensity distribution, P(bin) is displayed in Figure 4 and T is the mean temperature (global or tropical, land or ocean). The GPCP data is used to study the $dP_{\%}/dT$ variations globally and over the tropics, over ocean and land. The $dP_{\%}/dT$ response over the tropical ocean is fully investigated in the next section.

The $dP_{\%}/dT$ is calculated using the daily 1^o resolution data and the results are shown in Figure 5. Figure 5a is for the whole globe, the global ocean and the global land respectively. The solid dots represent the significant correlations after applying a two-tailed test using Pearson critical values at the significance level of 5%. All three areas show a positive precipitation response to warming over the higher percentile bins and negative responses over the lower bins. However, only the global and global ocean responses for the heavier precipitation bins are statistically significant. There is no significant response over the global land at all and the response over the highest percentile bins is close to zero, due to complicated response mechanisms over different land areas [*Trenberth and*

Shea, 2005; *Haerter et al.*, 2010]. Specifically, cause and effect is ambiguous: for some regions, less cloud and rainfall with lower soil moisture is associated with enhanced surface heating by solar radiation while over other regions, with ample moisture availability, warmer temperatures may be associated with more low level water vapor and higher precipitation intensity. The response over the global ocean is thus higher than that over the whole globe.

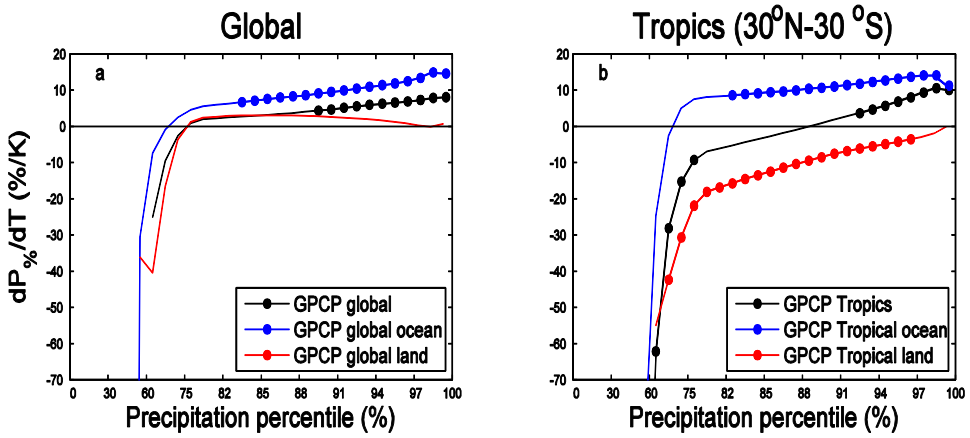

Figure 5. $dP_{\%}/dT$ over precipitation percentile bins. (a) over the global, the global ocean and the global land; (b) over the Tropics, the tropical ocean and the tropical land. They are calculated using the daily data at the 1^{o} resolution of GPCP dataset from 1998 to 2008.

The tropics show a similar behavior to the global response although the threshold separating the positive and negative responses is over higher percentile bins (approximately 88%) than that for the global (around 75%). The land response is predominantly negative (warmer tropical land temperature is associated with less rainfall) and statistically significant; similar results are given by the TRMM 3B42 dataset (not shown here).

6. Influence of temporal and spatial averaging on observed precipitation responses over the tropical ocean

Over the tropical oceans, there are many satellite-based observational precipitation datasets available which display contrasting precipitation responses [*John et al.*, 2009]. Therefore it is important to understand the reasons for discrepancies and, if possible, identify the most physically robust dataset. Based upon the analysis of the precipitation percentile distributions, one hypothesis is that varying temporal and spatial resolutions may affect the analysis results, since this fundamentally impacts the precipitation intensity distribution. In order to investigate these resolution effects on the precipitation response to the surface temperature change, the $dP_{\%}/dT$ values over the tropical ocean are calculated for different datasets at different temporal and spatial resolutions, where P is the precipitation for each percentile bin and T is tropical ocean mean temperature. For comparison purpose, the data period used for the calculation in this section is from 1998 to 2008, except for AMSRE which is from 2003-2010.

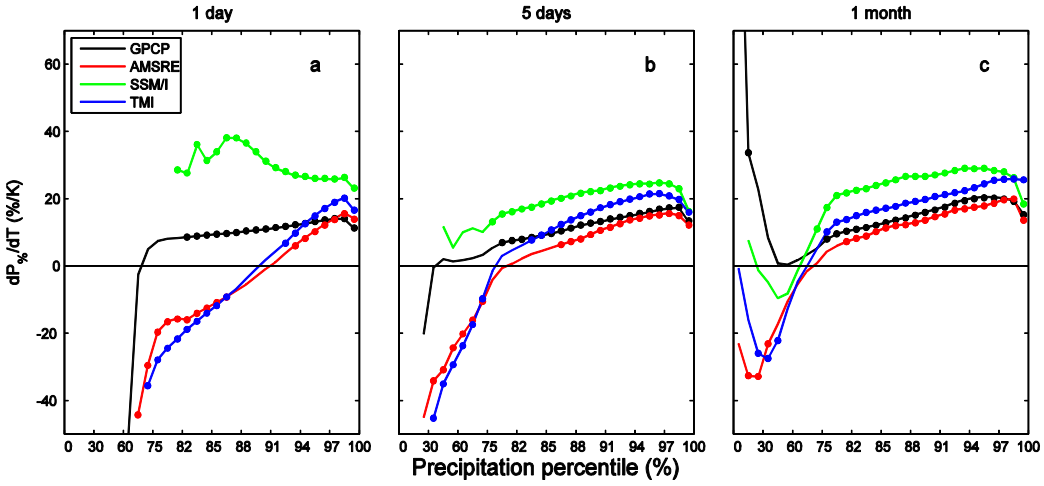

Figure 6. Relative precipitation changes over the tropical ocean at different percentile bins. Temporal integrations are one day, five days and one month respectively and all datasets are at 1° resolution. The dots show the points where the correlations between precipitation and temperature anomalies are significant after applying a two-tailed test using Pearson critical values at the level of 5%. The data period used for this calculation is from 1998 to 2008, except for AMSRE dataset which is from 2003-2010.

a. Temporal resolution effect

To investigate the temporal resolution effect on the $dP_{\%}/dT$ calculation, only four datasets (GPCP, AMSRE, SSM/I and TMI) are considered since the observational period of SSMIS datasets (F16 and F17) are too short and the TRMM 3B42 and HOAPS datasets displays inconsistent variability (Figure 2c).

They are all integrated to 1° resolution and also to 1 day, 5 days and a month, respectively. The $dP_{\%}/dT$ is calculated and the results are plotted in Figure 6. The solid dots are significant points as stated before. For daily data, three out of four datasets lines show negative response at lower percentile bins though the negative response from GPCP dataset is not significant due to weak correlations. All datasets show positive response at high percentile bins. This is consistent with the dry region becoming drier and the wet region is becoming wetter with warming [*John et al*., 2009; *Allan et al.*, 2010; *Zhou et al.*, 2011] due to enhanced moisture transports [*Held and Soden*, 2006]. The $dP_{\%}/dT$ from SSM/I is always positive because the SSM/I data are less sensitive to light precipitation and have large percentage of zero precipitation grid points (see Figure 4a).

For both AMSRE and TMI datasets, there are significant negative correlations and the threshold points separating the positive and negative correlations for those two datasets are very close, but in general the threshold point position depends on the datasets and the integrations.

Averaging from 1 to 5-days increases the consistency precipitation distribution response to tropical warming between datasets. The threshold bin position separating the positive and negative correlations shifts from high

percentile bins to low percentile bins due to the averaging effect. For the one month integration, the results are similar to the five day integration, but it becomes noisier over the low percentile bins, presumably due to averaging over contrasting dynamical situations.

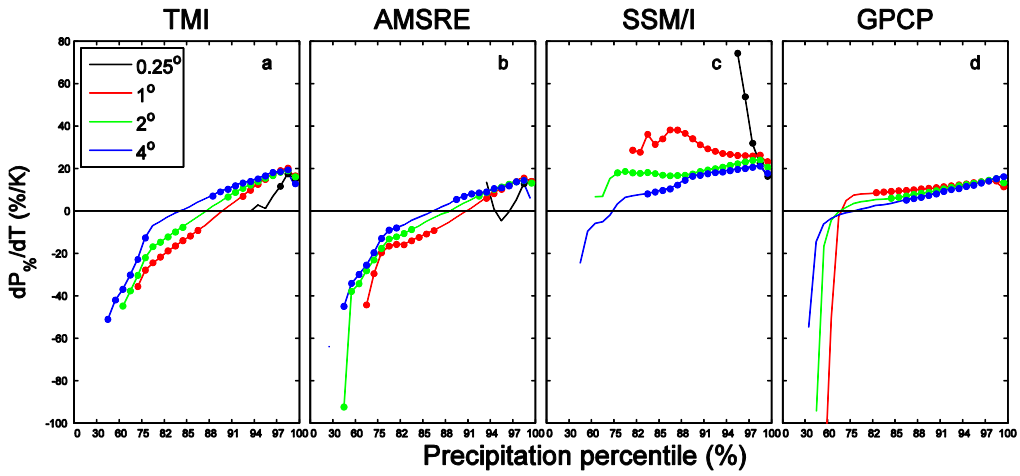

Figure 7. Spatial integration effect on precipitation and temperature relations over the tropical ocean from daily datasets of TMI, AMSRE, SSM/I and GPCP.

b. Spatial resolution effect

The spatial integration effect on $dP_{\%}/dT$ is also investigated using the daily data and plotted in Figure 7. For TMI, AMSRE and SSM/I datasets, there are four resolutions of 0.25^o, 1^o, 2^o and 4^o, but there are only three resolutions of 1^o, 2^o and 4^o for GPCP. For the TMI data (Figure 7a), the spatial integration effect on the precipitation response to the temperature is obvious, the threshold bin position shifts to the smaller percentile bins and the negative correlation over the dry regions becomes significant. The results for AMSRE (Figure 7b) are similar to that of TMI. Spatial averaging has a similar effect to the temporal averaging shown in Figure 6. The spatial integration effect on SSM/I data (Figure 7c) is also profound, particularly between the 0.25^o and 1^o resolutions, but the effect on GPCP data is relatively small (Figure 7d). This may be because the GPCP dataset combines multi-satellite products and some spatiotemporal integration may have been implicitly applied during processing. Based on this analysis, it appears that the GPCP, TMI and AMSRE datasets are reasonably consistent in their characteristics.

c. Threshold

Both temporal and spatial integrations have profound effects on the study of precipitation response to temperature. The threshold precipitation percentile bins separating the negative and positive responses are plotted in Figure 8. Figure 8a is the threshold variation with time integration period for three datasets (GPCP, AMSRE and TMI) over the tropical ocean at 1^o resolution. Both AMSRE and TMI agree well, but the GPCP has a lower threshold, again thought to relate to the more complex methodology applied to this dataset. The spread of the threshold value due to time integration is comparable with that of using different datasets. Figure 8b is from TMI for different spatial integrations. The spatial integration effect is smaller than that of time integration. The influence of resolution on the precipitation percentile threshold below which negative dP/dT occurs is strong for the daily data (Figure 8b, inset). As expected, both temporal and spatial integrations reduce the frequency of high and zero precipitation rates, therefore shifting the threshold bin to the lower end of the precipitation distribution.

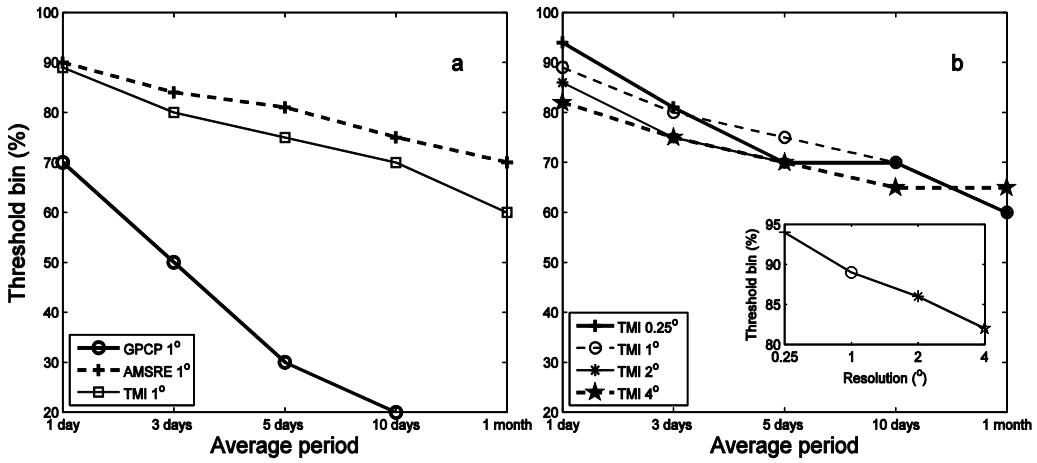

Figure 8. Threshold separating the negative and positive precipitation response to the temperature. The left panel is from three daily datasets at 1^o resolution and the right panel is from TMI daily data at different resolutions.

d. Dry and wet regions

Previous studies have highlighted the contrasting responses of the tropical wet and dry regions [*Chou et al.,* 2007; *Allan et al.*, 2010] although the precise threshold in the distribution below which negative dP/dT occur appears to be sensitive to time-averaging (previous sections; *Pall et al.,* 2007). Here, we extend the analysis of the previous section to analyse in more detail the influence of time-integration upon the precipitation percentile threshold and the results are plotted in Figure 9. The calculations are carried out using daily, 5-day and monthly data at 1^o spatial resolution from the TMI dataset. The integration on the left panel (Figure 9a) is from the first precipitation percentile bin (0%) to a variable percentile bin used as the x-axis (hereafter 0-bin integration). The integration on the right panel (Figure 9b) is from a variable percentile bin to percentile100 (hereafter bin-100 integration). For the 0-bin

integration, the first few data points represent the relationship between precipitation and temperature over the dry regime. It is clear that the correlation is negative until percentile 96% for the daily integration, slightly higher than the value found by *Pall et al.* [2007] for climate model data. The temporal integration greatly reduces the negative correlation and shifts the threshold location to the much lower percentile bins, as suggested by *Allan et al.* [2010]. For daily integration there is big jump over the first few valid data points where the non-zero precipitation begins. The variation of this location causes the big jump due to lower value of mean precipitation and big standard deviation over these percentile bins (75-82%).

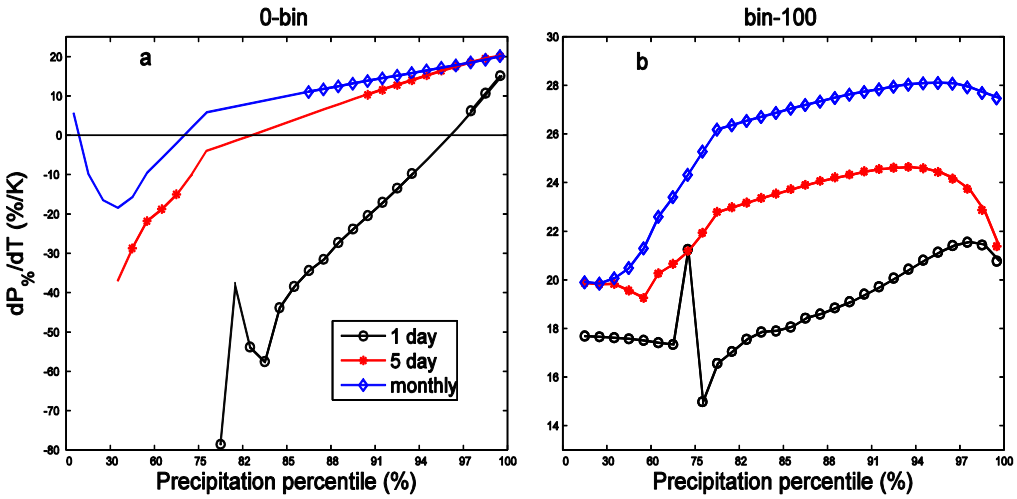

Figure 9. $dP_{\%}/dT$ calculated from TMI data with 1^{o} resolution for integration period of 1 day, 5days and one month. Left panel is integrated from the first percentile bin (0%) to a variable percentile bin, the right panel is integrated from a variable percentile bin to percentile 100. The X axis is the variable percentile bin. As before, the symbols represent points having significant correlations between precipitation and the temperature.

For the bin-100 integration, the first data points are identical to the last data points of 0-bin integration (both are tropical ocean mean). They are the relations for total precipitation and temperature. Over the big percentile bins on the right end, the relations are for the heaviest precipitation and they are significantly positive as shown in Figures 6 and 7. As explained, the jumps happen when non-zero precipitation rate starts for daily integrated data. It is clearly seen that time-integration of the data explains the reduction of this critical threshold from around the 96^{th} percentile for daily data down to around the 60^{th} percentile for monthly data (Figure 9a). Again, the "daily" satellite data may behave more like hourly snap-shots; using model daily data, *Pall et al.* [2007] found the threshold to be closer to the 90^{th} percentile of precipitation intensity.

7. Summary

Climate model projections of substantial future changes in intense precipitation and drought are of immediate concern to society [*Meehl et al.,* 2007]. Though the variations and responses of precipitation on the interannual time scale might be quite different from those on the decadal and long-term time scales given likely different physical mechanisms, it is still important to be able to verify and understand the physical processes responsible for these anticipated changes through careful use of well-calibrated and well-characterized observing systems. While rain gauge data provides "ground truth" [*Zhang et al.,* 2007; *Min et al.,* 2011] their global coverage is somewhat limited and increasingly the use of satellite measurements in detecting rainfall changes is becoming an essential component of the verification process [*Huffman et al.,* 2009; *Maidment et al.,* 2011]. However, substantial discrepancies exist between satellite datasets [*Quartly et al.,* 2007; *John et al.,* 2009] and this motivates detailed analysis of the reasons for uncertain rainfall responses to current climate variability [*Wentz et al*., 2007; *Liepert and Previdi*, 2009; *Arkin et al.,* 2010]. In the present study, interannual variability of precipitation from multiple satellite datasets and blended satellite data products are compared to attempt to understand the causes of discrepancies and to detect robust, physically reasonable responses. Our main focus is on interannual co-variability of precipitation and surface temperature over the globe and tropical land and oceans.

Over the period 1998-2008, global P is found to increase at around 6%/K from SSM/I-based products (e.g. GPCP), of similar magnitude to that found by *Wentz et al.* [2007] but larger than estimated by *Adler et al.* [2008]. The time period is too short to reliably detect responses relevant for climate change [*Liepert and Previdi*, 2009] yet is a useful and physically-based metric to consider [*Held and Soden*, 2006]. Much of the response is determined by strong co-variability in tropical ocean P and T (dP/dT ranges from 10-30%/K depending upon time-period and dataset) which is offset by anti-correlation over land of around –10%/K, consistent with previous analysis [*Wang et al.*, 2008]. In agreement with previous studies, warming during El Nino is associated with greater precipitation over the tropical oceans and less rainfall over land [*Adler et al.*, 2008; *Gu et al.,* 2007; *Wang et al*., 2008]; cause and effect over land is ambiguous since over some regions, less cloud and rain is conducive to enhanced surface heating while over moist tropical regimes, warmer temperatures may be associated with more convective rainfall [*Trenberth and Shea*, 2005].

Variability between TRMM TMI, SSM/I, GPCP and AMSRE datasets is generally consistent over the tropical ocean over the period 1997-2008 but the HOAPS dataset appears to overestimate the magnitude and the TRMM 3B42 dataset produces unrealistic variability. It will be useful to include TRMM radar precipitation data in future studies as both TRMM TMI and TRMM PR have good agreement [*Lau and Wu*, 2011]. Over the land, GPCP and TRMM 3B42 are in reasonable agreement. However, it is noted that many of the datasets are not independent of one another.

Comparing the intensity distribution of P and its response to interannual changes in surface temperature between datasets reveals large differences. The heaviest percentiles of P over the tropical ocean become more intense with warming in all datasets at the rate of about 15-20%/K, consistent with some land-based estimates [*Lenderink and van Meijgaard*, 2010] and with modeling studies [*Sugiyama et al.,* 2010]. At lower P percentiles there are large

differences between datasets although below the 80th percentile of daily P intensity the AMSR-E and TMI estimates exhibit a significant decline in P intensity with warming. The GPCP, TMI and AMSRE datasets appear reasonably consistent in the characteristics of rainfall intensity responses to surface temperature changes.

To understand the reasons for the differing responses amongst datasets, the time and space averaging is analysed, motivated by the sizable differences in mean precipitation intensity distributions amongst datasets and its dependence upon spatial and temporal resolution. Time-averaging of the data, and to a lesser extent, spatial integration of the data leads to (i) greater agreement between datasets and (ii) a reduction of the critical precipitation percentile threshold, below which precipitation intensity generally declines with warming. Based upon this analysis, there is some indication that blended products such as GPCP have introduced an implicit spatial and temporal averaging effect upon the data, such that the 1 degree daily data may in reality represent a larger spatial and temporal average. It should also be noted that although we term the 0.25 degree satellite estimates as daily data, in fact these are snap-shots coinciding with satellite overpasses and are therefore closer to hourly estimates [*Field and Shutts*, 2009; *Wilcox and Donner*, 2008].

We find that choosing a spatial resolution of 1 degree and time-averaging of 5-days increases consistency between datasets, compared to 0.25 degree daily data, and may be the most useful scales to consider in comparing with the climate model outputs. For this configuration, the precipitation intensity bin threshold, separating the contrasting wet and dry regime responses to warming/cooling cycles is around the 80th percentile for AMSR-E and TMI but is less coherent and lower (30%) for GPCP data. Considering the wet and dry regimes separately, separated by the 60th P percentile, the 5-day average, 1 degree TMI data exhibits a coherent drying of the dry regime at the rate of -20%/K and the wet regime becomes wetter at a similar rate (just below 20%/K). In future work we hope to apply these techniques to assess the responses of climate model simulations of daily precipitation using the GPCP and microwave-based datasets (e.g. TMI, AMSR-E) described in the current paper. It will also be important to consider the physical basis for such changes, for example, relating to moisture transport [*Held and Soden*, 2006; *Sohn and Park*, 2010; Zahn and Allan, 2011] and energetic considerations [*Muller and O'Gorman*, 2011] including the influence of aerosol [*Andrews et al.*, 2010; *Ming et al.*, 2010].

Acknowledgements. This work was undertaken as part of the PAGODA and PREPARE projects funded by the UK Natural Environmental Research Council under grants NE/I006672/1 and NE/G015708/1 and was supported by the National Centre for Earth Observations and the National Centre for Atmospheric Science. GPCP data were extracted from http://www.gewex.org/gpcpdata.htm, AMSRE, SSM/I, SSMIS and TMI data from ftp.ssmi.com, HOAPS data from http://www.hoaps.zmaw.de/ and TRMM 3B42 data from http://mirador.gsfc.nasa.gov/. The scientists involved in the generation of these datasets are sincerely acknowledged. The authors would like to thank three anonymous reviewers for providing constructive comments on the paper.

8. References

Adler, R.F., G. Gu, G.J. Huffman, J.J. Wang, S. Curtis, and D.T. Bolvin (2008), Relationships between global precipitation and surface temperature on interannual and longer timescales (1979-2006), *J. Geophys. Res.*, *113* (D22104), doi: 10.1029/2008JD010536.

Adler, R.F., G.J. Huffman, A. Chang, R. Ferraro, P. Xie, J. Janowiak, B. Rudolf, U. Schneider, S. Curtis, D. Bolvin, A. Gruber, J. Susskind, and P. Arkin (2003), The Version 2 Global Precipitation Climatology Project (GPCP) Monthly Precipitation Analysis (1979-Present), *J. Hydrometeor., 4*, 1147-1167.

Allan, R. P. (2009), Examination of Relationships between Clear-Sky Longwave Radiation and Aspects of the Atmospheric Hydrological Cycle in Climate Models, Reanalyses, and Observations, *J. Climate, 22*, 3127-3145.

Allan, R. P., B. J. Soden, V. O. John, W. Ingram, and P. Good (2010), Current changes in tropical precipitation, *Environ. Res. Lett.*, 5, 025205, doi:10.1088/1748-9326/5/2/025205.

Andersson, A., K. Fennig, C. Klepp, S. Bakan, H. Graßl, and J. Schulz (2010), The Hamburg Ocean Atmosphere Parameters and Fluxes from Satellite Data - HOAPS-3, *Earth Syst. Sci. Data Discuss.*, *3*, 143-194, doi:10.5194/essdd-3-143-2010.

Andrews, T., P. M. Forster, O. Boucher, N. Bellouin, and A. Jones (2010), Precipitation, radiative forcing and global temperature change, *Geophys Res Lett 37*, L14701, doi:10.1029/2010GL04399.

Arkin, P. A., T. M. Smith, M. R. P. Sapiano, and J. Janowiak (2010), The observed sensitivity of the global hydrological cycle to changes in surface temperature, *Environ. Res. Lett.* 5:035201. doi:10.1088/17489326/5/3/035201.

Bengtsson, L., K. Hodges, and N. Keenlyside (2007), Will Extratropical Storms Intensify in a Warmer Climate, *J. Climate, 22*, 2276-2301, doi: 10.1175/2008JCLI2678.1.

Chou, C., J.-Y. Tu, and P.-H. Tan (2007), Asymmetry of tropical precipitation change under global warming, *Geophys. Res. Lett., 34*, L17708, doi:10.1029/2007GL030327.

Dee, D. P. et al. (2011), The ERA-Interim reanalysis: Configuration and performance of the data assimilation system, *Q.J. Roy. Meteorol. Soc.*, *137*, 553-597. doi:10.1002/qj.828.

Emori, S., and S. J. Brown (2005), Dynamic and thermodynamic changes in mean and extreme precipitation under changed climate, *Geophys. Res. Lett., 32*, L17706, doi:10.1029/2005GL023272.

Field, P. R., and G. J. Shutts (2009), Properties of normalised rain-rate distributions in the tropical Pacific, *Q. J. R. Meteorol. Soc. 135* 175–8.

Gastineau, G., and B. J. Soden (2011), Evidence for a weakening of tropical surface wind extrmes in response to atmospheric warming, *Goephys. Res. Lett., 38*, L09706, doi:10.1029/2011HL047138.

Gu, G., R. F. Adler, G. J. Huffman, and S. Curtis (2007), Tropical rainfall variability on interannual-to-interdecadal and longer time scales derived from the GPCP monthly product, *J. Climate, 20*, 4033–404.

Haerter, J. O., P. Berg, and S. Hagemann (2010), Heavy rain intensity distributions on varying time scales and at different temperatures, *Geophys. Res. Lett. 115*, D17102, doi:10.1029/2009JD013384.

Held, I., and B. J. Soden (2006), Robust responses of the hydrological cycle to global warming. *J. of Climate, 19(21),* 5686-99, doi:10.1175/JCLI3990.1.

Huffman, G.J., et al. (2007), The TRMM Multisatellite Precipitation Analysis (TMPA): Quasi-Global, Multiyear, Combined-Sensor Precipitation Estimates at Fine Scales, *J. Hydrometeor*..

Huffman, G.J., R.F. Adler, D.T. Bolvin and G. Gu (2009), Improving global precipitation record: GPCP version 2.1, *Geophys. Res. Lett.*, *36*, L17808, doi:10.1029/2009GL040000

John, V. O., R. P. Allan, and B. J. Soden (2009), How robust are observed and simulated precipitation responses to tropical ocean warming?, *Geophys. Res. Lett.*, *36*, L14702, doi:10.1029/2009GL038276.

Lambert, F. H., and M. J. Webb (2008), Dependency of global mean precipitation on surface temperature, *Geophys. Res. Lett.*, *35*, 16.

Lau, K. M., and H. T. Wu (2011), Climatology and changes in tropical oceanic rainfall characteristics inferred from Tropical Rainfall Measuring Mission (TRMM) data (1998–2009), *J. Geophys. Res.*, *116*, D17111, doi:10.1029/2011JD015827.

Lenderink, G., and E. van Meijgaard (2010), Linking increases in hourly precipitation extremes to atmospheric temperature and moisture changes, *Environ. Res. Lett. 5*, 025208.

Liepert, B. G., and M. Previdi (2009), Do models and observations disagree on the rainfall response to global warming? *J. Climate, 22*, 3156–6.

Lobl, E. (2001), Joint Advanced Microwave Scanning Radiometer (AMSR) Science Team meeting. *Earth Observer 13(3)*: 3-9.

Maidment, R. I., D. I. F. Grimes, R. P. Allan, H. Greatrex, O. Rojas, O. Leo (2011), Evaluation of satellite-based and model re-analysis rainfall estimates for Uganda, submitted to *Meteorological Applications.*

Meehl, G. et al. (2007), Global climate projections Climate Change 2007: The Physical Science Basis. Contribution of Working Group I to the Fourth Assessment Report of the Intergovernmental Panel on Climate Change ed S Solomon, D Qin, M Manning, Z Chen, M Marquis, K B Averyt, M Tignor and H L Miller (Cambridge: Cambridge University Press) pp 747–845.

Min, S.-K., X. Zhang, F. W. Zwiers, and G. C. Hegerl (2011), Human contribution to more-intense precipitation extremes, *Nature 470*, 378–381.

Ming, Y., V. Ramaswamy, and G. Persad (2010), Two opposing effects of absorbing aerosols on global-mean precipitation, Geophys. Res. Lett., 37, L13701, doi:10.1029/2010GL042895.

Mitchell, J., C. A. Wilson, and W. M. Cunnington (1987), On CO2 climate sensitivity and model dependence of results, *Quart J Roy Meteorol Soc 113*, 293–32.

Muller, C. J., and P. A. O'Gorman (2011), An energetic perspective on the regional response of precipitation to climate change, *Nature Climate Change 1*, 266-271.

O'Gorman, P.A., and T. Schneider (2009), The physical basis for increases in precipitation extremes in simulations of 21st-century climate change, *Proceedings of the National Academy of Sciences* 106, 14773-14777.

Pall, P., M. R. Allen, and D. A. Stone (2007), Testing the Clauius Clapeyron constraint on changes in extreme precipitation under CO2 warming, *Climate Dynamics 28*, 351–36.

Quartly, G. D., E. A. Kyte, M. A. Srokosz, and M. N. Tsimplis (2007), An intercomparison of global oceanic precipitation climatologies, *J. Geophys. Res.*, *112*, D10121, doi:10.1029/2006JD007810.

Sohn, B. J.,S. C. Park (2010), Strengthened tropical circulations in past three decades inferred from water vapor transport, *J Geophys Res 115*, D15112, doi:10.1029/2009JD01371.

Stephens, G. L., and T. D. Ellis (2008), Controls of global-mean precipitation increases in global warming GCM experiments, *J. Climate*, *21*, 6141–5.

Sugiyama, M., H. Shiogama, and S. Emori (2010), Precipitation extreme changes exceeding moisture content increases in MIROC and IPCC climate models, *Proc Nat Acad Sci 107*, 571–57.

Trenberth, K. E., and D. J. Shea (2005), Relationships between precipitation and surface temperature, *Geophys. Res. Lett.*, *32*, L14703, doi:10.1029/2005GL022760.

Trenberth, K. E. (2011), Changes in precipitation with climate change, *Climate Research, 47*, 123-138, doi:10.3354/cr00953.

Vila D., D. R. Ferraro, and H. Semunegus (2010), Improved Global Rainfall Retrieval using the Special Sensor Microwave Imager (SSM/I), *J. Appl. Meteor. Climatol.*, *49*, 1032–1043. doi: 10.1175/2009JAMC2294.1.

Wang, J.-J., R. F. Adler, and G. Gu (2008), Tropical rainfall-surface temperature relations using Tropical Rainfall Measuring Mission precipitation data, *J. Geophys. Res.*, *113*, D18115, doi:10.1029/2007JD009540.

Wentz, F. J., and R. W. Spencer (1998), SSM/I Rain Retrievals within a Unified All-Weather Ocean Algorithm, *J. Atmos. Sci*., *55*, 1613-1627.

Wentz, F. J., L. Ricciardulli, K. Hilburn, and C. Mears (2007), How Much More Rain Will Global Warming Bring? *Science, 317*, 233–5.

Wilcox, E. M., andL. J. Donner (2007), The frequency of extreme rain events in satellite rain-rate estimates and an atmospheric general circulation model, *J. Clim.*, *20*, 53–6.

Zahn, M., and R. P. Allan, (2011) Changes in water vapor transports of the ascending branch of the tropical circulation, *J. Geophys. Res. 116*, D18111, doi:10.1029/2011JD016206.

801 Zhang, X., F. W. Zwiers, G. C. Hegerl, F. H. Lambert, N. P. Gillett, S. Solomon, P. A. Stott, and T.
802 Nozawa (2007), Detection of human influence on twentieth-century precipitation trends. *Nature*, *448*, 461–
803 465.
804
805 Zhou, Y.P., K.-M. Xu, Y. C. Sud, and A. K. Betts (2011), Recent trends of the tropical hydrological cycle
806 inferred from Global Precipitation Climatology Project and International Satellite Cloud Climatology
807 Project data, *J. Geophys. Res.*, *116*, D09101, doi:10.1029/2010JD015197.
808

809 Figure captions

810

811 **Figure 1**. Mean seasonal cycle of. (a) temperatures over the globe, the tropical ocean and the tropical land based on
812 the reference period of 2003-2008 (10^{o}C is added to the global temperature to improve the clarity of the plot) and
813 precipitation for different datasets based on the reference period of 2003-2008 except for HOASPS (based on 2000-
814 2005), SSMIS F16 dataset (based on 2004-2009) and the SSMIS F17 dataset (based on 2007-2010) over (b)
815 the globe, (c) the tropical ocean, and (d) the tropical land.

816 **Figure 2**. Deseasonalised anomalies of temperature and precipitation relative to the mean values of Figure 1: (a)
817 temperature anomalies at 2m from ERA INTERIM dataset over the globe, the tropical ocean and the tropical land .
818 Precipitation anomalies (b) over the globe, (c) over the tropical ocean, and (d) over the tropical land for all datasets.
819 All curves are plotted with three month running mean. The amplitude of HOAPS precipitation anomalies are scaled
820 down by a factor of 3 to improve the clarity of the plot.

821 **Figure 3**. Scatter plot showing correlations between precipitation and temperature anomalies (a) over the global, (b)
822 the tropical ocean and (c) the tropical land.
823

824 **Figure 4**. Mean tropical ocean precipitation over the reference period of Figure 1 in different precipitation
825 percentile bins. The upper row is for different datasets at 1^{o} resolution and the lower row is for TMI dataset at
826 different spatial resolutions.

827 **Figure 5**. $dP_{\%}/dT$ over precipitation percentile bins. (a) over the global, the global ocean and the global land; (b)
828 over the Tropics, the tropical ocean and the tropical land. They are calculated using the daily data at the 1^{o} resolution
829 of GPCP dataset from 1998 to 2008.
830

831 **Figure 6**. Relative precipitation changes over the tropical ocean at different percentile bins. Temporal integrations
832 are one day, five days and one month respectively and all datasets are at 1^{o} resolution. The dots show the points
833 where the correlations between precipitation and temperature anomalies are significant after applying a two-tailed
834 test using Pearson critical values at the level of 5%. The data period used for this calculation is from 1998 to 2008,
835 except for AMSRE dataset which is from 2003-2010.
836

837 **Figure 7**. Spatial integration effect on precipitation and temperature relations over the tropical ocean from daily
838 datasets of TMI, AMSRE, SSM/I and GPCP.
839

840 **Figure 8**. Threshold separating the negative and positive precipitation response to the temperature. The left panel is
841 from three daily datasets at 1^{o} resolution and the right panel is from TMI daily data at different resolutions.
842

843 **Figure 9**. $dP_{\%}/dT$ calculated from TMI data with 1^{o} resolution for integration period of 1 day, 5days and one month.
844 Left panel is integrated from the first percentile bin (0%) to a variable percentile bin, the right panel is integrated
845 from a variable percentile bin to percentile 100. The X axis is the variable percentile bin. As before, the symbols
846 represent points having significant correlations between precipitation and the temperature.
847